Functional beamforming applied to imaging of fly-over noise on landing aircraft

Merino Martinez, Roberto; Snellen, Mirjam; Simons, Dick

DOI
10.2514/1.C033691

Publication date
2016

Document Version
Accepted author manuscript

Published in
Journal of Aircraft: devoted to aeronautical science and technology

Functional Beamforming Applied to Imaging of Fly-Over Noise on Landing Aircraft

Roberto Merino-Martínez[a], Mirjam Snellen[b] and Dick G. Simons[c]
Delft University of Technology, 2629 HS Delft, the Netherlands

Functional beamforming is a state-of-the-art nonlinear algorithm based on the conventional frequency domain beamformer. In general, it is found to provide improved array spatial resolution and dynamic range. The computational time required for the functional beamforming is approximately the same as that for the conventional frequency domain beamformer and, in general, notably shorter than those of the deconvolution methods. In this paper, several simulations are presented comparing the performance of this algorithm with other imaging methods. Moreover, this beamforming technique is applied to 115 fly-over measurements performed with a 32 microphone array on landing aircraft. The simulated and experimental results show good agreement. It is found that for both synthetic and experimental data, functional beamforming offers better quality acoustic images, with a dynamic range (i.e. the difference in dB between the main lobe and the highest sidelobe) approximately 30 times larger and an array spatial resolution (i.e. the width of the main lobe 3 dB below its peak) approximately 6 times better than the conventional frequency domain beamformer. All these factors indicate that functional beamforming is a very promising algorithm for processing acoustic array data.

[a] PhD candidate, Aircraft Noise & Climate Effects section, Faculty of Aerospace Engineering, Kluyverweg 1. AIAA Student Member. E-mail: r.merinomartinez@tudelft.nl

[b] Associate professor, Aircraft Noise & Climate Effects section, Faculty of Aerospace Engineering, Kluyverweg 1. E-mail: m.snellen@tudelft.nl

[c] Full professor, Aircraft Noise & Climate Effects section, Faculty of Aerospace Engineering, Kluyverweg 1. E-mail: d.g.simons@tudelft.nl

Nomenclature

$\boldsymbol{C}$ = $N \times N$ Cross Spectral Matrix (CSM)

$\boldsymbol{g}$ = $N \times 1$ Steering vector

$\boldsymbol{I}$ = $N \times N$ Identity matrix

$\boldsymbol{M}$ = Mach number vector

$\boldsymbol{p}$ = $N \times 1$ vector containing the Fourier-transformed recorded pressures at each microphone

$\boldsymbol{U}$ = $N \times N$ Unitary matrix whose columns are the eigenvectors of the Cross Spectral Matrix

$\boldsymbol{u}$ = $N \times 1$ Eigenvectors of the Cross Spectral Matrix

$\boldsymbol{V}$ = Source velocity vector

$\boldsymbol{w}$ = $N \times 1$ Normalized steering vector

$\boldsymbol{x}$ = Position vector for each microphone in the array

A = Source autopower

c = Sound speed

D = Microphone array diameter

f = Sound frequency

h = Distance from the sound source to the microphone array

i = $\sqrt{-1}$

j = Scan point index

k = Scan point index

m = Scan point index

N = Number of microphones in the array

n = Microphone index

p = Recorded pressure at each microphone

R = Minimum resolvable distance according to the Rayleigh limit

s = Sound source amplitude

x = X coordinate from the centre of the array

y = Y coordinate from the centre of the array

z = Z coordinate from the centre of the array

CFDBF = Conventional Frequency Domain Beamforming

CLEAN-PSF = CLEAN method based on PSF's

CLEAN-SC = CLEAN method based on source coherence

CSM = Cross Spectral Matrix

DAMAS = Deconvolution Approach for the Mapping of Acoustic Sources

PSF = Point Spread Function

RAB = Robust Adaptive Beamforming

SINR = Signal-to-Interference Ratio

SPL = Sound Pressure Level

$\boldsymbol{\xi}$ = Scan point position vector

$\boldsymbol{\Sigma}$ = $N \times N$ Diagonal matrix whose diagonal elements are the eigenvalues of the CSM

β = $\sqrt{1 - \|\boldsymbol{M}\|^2}$

Δt = Time delay between the emission and the reception by the observer

ϵ = Diagonal loading factor (RAB method)

θ = Angle between the relative position vector of the source with respect to the observer and $\boldsymbol{V}$

λ = Sound signal wavelength

μ = Diagonal loading parameter (RAB method)

ν = Exponent parameter (Functional Beamforming method)

σ = Eigenvalues of the CSM

ϕ = Angle between two steering vectors in the N-dimensional vector space

φ = Minimum resolvable angular distance according to Rayleigh criterion

I. Introduction

The continuous increase of air traffic and stricter noise regulations have caused that aircraft noise is one of the main issues which the aviation industry has to currently deal with. In fact, for many airports, noise restrictions are nowadays the limiting factor when increasing capacity. Engine noise has decreased significantly on modern aircraft, to such an extent that airframe noise, which is produced by the interaction of the aerodynamic surfaces and the surrounding turbulent flow [1],

can have roughly the same sound pressure level as engine noise. This phenomenon is particularly noticeable during landing, when the engines operate at low thrust. In addition, the high lift devices (such as the flaps and slats) and landing gear are extended. In order to further reduce the noise emissions, it is essential to precisely know all the noise sources on an aircraft and their contributions to the total aircraft noise [2].

Microphone arrays are very useful tools for acoustic source localization. Due to the increasing computational capacity of computers and data acquisition systems, large numbers of microphones, high sample frequencies and long acquisition times, the current arrays provide detailed imaging capabilities. These devices can be employed in both stationary and moving source experiments, such as sources in wind tunnels or aircraft fly-overs, respectively. One of the main advantages of using microphone arrays in comparison to other tools, such as acoustic mirrors, is the short measurement time required, which enables cheaper experiments, especially in wind tunnels [3]. Fly-over tests with microphone arrays are the only method to accurately measure the sound sources of an aircraft in flight, which cannot be fully represented in wind tunnels or numerical simulations.

In order to obtain source location maps, also known as acoustic images, the microphone array data are processed with a beamforming algorithm, which estimates the location and strength of a signal of interest. Beamforming techniques are increasingly being used in the aerospace industry in order to support the development of noise reduction techniques [4–12]. In the case of fly-over measurements, the data generally have to be pre-processed to take into account the background noise, the propagation effects (geometrical spreading and atmospheric attenuation), ground reflection, the movement of the source and the Doppler effect [13, 14].

Recently a new beamforming technique was proposed, the so-called functional beamforming algorithm [15, 16]. It is based on the conventional beamforming method, but it has better array spatial resolution and less sidelobes. In this research 115 fly-overs were recorded using a 32 microphone array. Functional beamforming was applied to these measurements. Given the large distance between the aircraft and the array, high resolution is an essential requirement when the aim is to distinguish the different aircraft noise sources. In this sense and taking also into account its low computational demand which allows for considering large numbers of measurements, functional beamforming is a

very promising technique. To the best of the authors' knowledge, there is no previous work done, applying this algorithm to full-scale fly-over measurements yet.

To assess its performance, this method is compared with other beamforming algorithms, i.e. CLEAN-PSF, CLEAN-SC and robust adaptive beamforming. The beamforming methods employed in this research are briefly explained in section II, including the functional beamforming algorithm. As a first step in assessing the performance of the beamforming methods, a synthetic study was performed in section III. Section IV summarizes the experimental set-up and the aircraft trajectory estimation methods. Section V presents the results from the analysis of the fly-over measurements and finally section VI gathers all the conclusions.

II. Beamforming methods applied

A. Conventional Frequency Domain Beamforming (CFDBF)

The so-called conventional beamforming or delay-and-sum beamforming is probably the simplest and most robust beamforming algorithm and, therefore, it is the most widely used method for aeroacoustic experiments. This technique is based on the phase delays between the emission of the sound signal at the source and the received signals at each microphone. This method can be employed in the time domain or in the frequency domain, by evaluating a discrete Fourier transform to the data. The latter is widely used due to the lower computational time required and possibility of performing a frequency analysis.

However, the dynamic range (or sidelobe level, typically defined as the difference in dB between the main lobe and the highest sidelobe [17]) and the array spatial resolution (usually defined as the width of the main lobe 3 dB below its peak [18]) of the conventional beamforming method is notably limited, and the presence of numerous sidelobes usually becomes a problem, especially at high frequencies. The array spatial resolution is, however, not strictly the same as the ability to separate multiple sound sources closely spaced emitting at the same frequency [18].

The CFDBF algorithm considers the Fourier transform of the recorded pressure amplitudes in each of the N microphones of the array as a N-dimensional vector, $\boldsymbol{p}(f) \in \mathbb{C}^{N\times 1}$, with frequency (f) dependence:

$$\boldsymbol{p}(f) = \begin{pmatrix} p_1(f) \\ \vdots \\ p_N(f) \end{pmatrix} \tag{1}$$

Assuming a stationary source in scan point $\boldsymbol{\xi}_j$, the received signal is modelled as $s_j \boldsymbol{g}_j$, where s_j is the source strength and $\boldsymbol{g}_j \in \mathbb{C}^{N\times 1}$ is the so-called steering vector. The steering vector has N components, $g_{j,n}$, $n = 1...N$, which are the modeled pressure amplitudes at the microphone locations of a source at that grid point with unit strength [3]. For a stationary source, the steering vector is:

$$g_{j,n} = \frac{-\exp\left(-2\pi i f \Delta t_{j,n}\right)}{4\pi \left\|\boldsymbol{x}_n - \boldsymbol{\xi}_j\right\|} = \frac{-\exp\left(\frac{-2\pi i f \left\|\boldsymbol{x}_n - \boldsymbol{\xi}_j\right\|}{c}\right)}{4\pi \left\|\boldsymbol{x}_n - \boldsymbol{\xi}_j\right\|} \tag{2}$$

where $\|\cdot\|$ is the Euclidean norm of the vector, $i = \sqrt{-1}$, $\Delta t_{j,n}$ is the time delay between the emission and the reception of the signal by the observer, $\boldsymbol{x}_n = (x_n,\, y_n,\, z_n) \in \mathbb{R}^{N\times 3}$, $n = 1 \dots N$ are the locations of the N microphones and c is the sound speed.

In case of a moving source, an expression can be derived [17] that expresses $\Delta t_{j,n}$ as a function of $\boldsymbol{\xi}_j$, where $\boldsymbol{\xi}_j$ corresponds to the source location at the moment of the sound reception,

$$g_{j,n} = \frac{-\exp\left(\frac{-2\pi i f \left[-\boldsymbol{M}\cdot(\boldsymbol{x}_n - \boldsymbol{\xi}_j) + \sqrt{(\boldsymbol{M}\cdot(\boldsymbol{x}_n - \boldsymbol{\xi}_j))^2 + \beta^2 \left\|\boldsymbol{x}_n - \boldsymbol{\xi}_j\right\|^2}\right]}{c\beta^2}\right)}{4\pi \left\|\boldsymbol{x}_n - \boldsymbol{\xi}_j\right\| \left(1 - \|\boldsymbol{M}\| \cos\theta\right)^2} \tag{3}$$

The use of this expression eliminates the requirement of tracing back the location of the aircraft at the moment of emission. In Eq. 3, $\boldsymbol{M}$ is the Mach number vector $\boldsymbol{M} = (M_x,\, M_y,\, M_z) = \left(\frac{V_x}{c},\, \frac{V_y}{c},\, \frac{V_z}{c}\right) = \frac{\boldsymbol{V}}{c}$, $\boldsymbol{V}$ is the source velocity vector, θ is the angle between the relative position vector of the source with respect to the observer and the source velocity vector, and β is a parameter defined as

$$\beta = \sqrt{1 - \|\boldsymbol{M}\|^2} \tag{4}$$

After performing a least square minimization of the difference between the recorded pressures

vector, $\boldsymbol{p}$, and the modeled pressures for a source at grid point $\boldsymbol{\xi}_j$, $s_j \boldsymbol{g}_j$, an estimate for the source autopower at that point, A, is obtained as

$$A\left(\xi_j\right) = \frac{1}{2} \frac{\boldsymbol{g}_j^* \boldsymbol{p} \boldsymbol{p}^* \boldsymbol{g}_j}{\left\|\boldsymbol{g}_j\right\|^4} = \boldsymbol{w}_j^* \boldsymbol{C} \boldsymbol{w}_j \tag{5}$$

In the previous expression, an asterisk, $(\cdot)^*$, denotes complex conjugate transpose and $\boldsymbol{w}_j$ is

$$\boldsymbol{w}_j = \frac{\boldsymbol{g}_j}{\boldsymbol{g}_j \boldsymbol{g}_j^*} = \frac{\boldsymbol{g}_j}{\left\|\boldsymbol{g}_j\right\|^2} \tag{6}$$

$\boldsymbol{C}$ is the $N \times N$ Cross Spectral Matrix (CSM) of the measured pressures

$$\boldsymbol{C} = \frac{1}{2} \boldsymbol{p} \boldsymbol{p}^* \tag{7}$$

Now, considering the presence of a single source of strength s_k in the location $\boldsymbol{\xi}_k$ and assuming the received signal is $s_k \boldsymbol{g}_k$, the CSM becomes

$$\boldsymbol{C} = \frac{1}{2} s_k \boldsymbol{g}_k \boldsymbol{g}_k^* s_k = \frac{1}{2} s_k^2 \boldsymbol{g}_k \boldsymbol{g}_k^* \tag{8}$$

Substituting Eq. 8 in Eq. 5 shows that steering towards the correct source location ($\boldsymbol{\xi}_k$), indeed provides the source strength, i.e.

$$A\left(\boldsymbol{\xi}_k\right) = \boldsymbol{w}_k^* \boldsymbol{C} \boldsymbol{w}_k = \boldsymbol{w}_k^* \frac{1}{2} s_k^2 \boldsymbol{g}_k \boldsymbol{g}_k^* \boldsymbol{w}_k = \frac{1}{2} s_k^2 \frac{\boldsymbol{g}_k^* \boldsymbol{g}_k \boldsymbol{g}_k^* \boldsymbol{g}_k}{\left\|\boldsymbol{g}_k\right\|^4} = \frac{1}{2} s_k^2 \tag{9}$$

For a general location $\boldsymbol{\xi}_m$ with steering vector $\boldsymbol{w}_m$, the source strength multiplied by the array Point Spread Function (PSF) is obtained:

$$A\left(\boldsymbol{\xi}_m\right) = \boldsymbol{w}_m^* \boldsymbol{C} \boldsymbol{w}_m = \boldsymbol{w}_m^* \frac{1}{2} s_k^2 \boldsymbol{g}_k \boldsymbol{g}_k^* \boldsymbol{w}_m = \frac{1}{2} s_k^2 \frac{\left\|\boldsymbol{g}_m^* \boldsymbol{g}_k\right\|^2}{\left\|\boldsymbol{g}_m\right\|^4}, \tag{10}$$

The PSF is less than 1 in all points apart from the correct source location or any alias points, i.e. the so-called grading lobes. Around a true source location, it describes the shape of the main lobe,

which can be approximated as $\cos^2\phi$, where ϕ is the angle between $\boldsymbol{g}_m$ and $\boldsymbol{g}_k$ in the N-dimensional steering vector space. Outside the main lobe, there are usually several sidelobes with sound pressure levels (SPL) about 5 to 10 dB lower.

B. Deconvolution methods

Deconvolution methods typically post-process the source maps obtained by the CFDBF algorithm in order to provide more detailed and higher quality information about the individual sources. These techniques assume that the source map constists of a superposition of PSFs. Algorithms such as CLEAN-PSF [19, 20], CLEAN-SC [20] or DAMAS [21–24], considerably increase the dynamic range, i.e. they diminish the effect of sidelobes, and improve the array spatial resolution (the width of the main lobe). However, these methods can have difficulties when applied to imaging continuous source distributions, since they often produce reconstructions seeming to consist of individual point sources. In addition, they are more computationally expensive than the conventional method. The CLEAN-PSF method iteratively cleans the "dirty source map" obtained by the CFDBF by looking for the main lobes, eliminating the corresponding theoretical PSF, and replacing the main lobe with a clean beam until a stop criterion is met. The CLEAN-SC method performs the same way, except that the PSF is determined from the CFDBF beamforming map using the fact that the main lobes should be coherent with their sidelobes. Both CLEAN methods provide the same source levels as the CFDBF for the main lobes. One of the main drawbacks of the CLEAN-SC method is that several real sources emitting noise at the same frequency may be overlooked and considered as a single source. The performance of both CLEAN methods is evaluated in this paper. The Deconvolution Approach for the Mapping of Acoustic Sources (DAMAS) iteratively solves an inverse problem for obtaining estimates for the sound sources at each grid point. This method is not applied in the current research.

C. Robust Adaptive Beamforming (RAB)

Adaptive beamforming [25, 26], also known as Capon beamforming [27], was developed in order to achieve better array resolution and lower and less sidelobes than the CFDBF.

The fundamental concept of the Capon beamforming technique is to obtain the beamforming

weight vector which maximizes the signal-to-interference ratio (SINR) [25]. Solving this linearly constrained quadratic problem leads to

$$\boldsymbol{w}_{Capon,j} = \frac{\boldsymbol{C}^{-1}\boldsymbol{g}_j}{\boldsymbol{g}_j^* \boldsymbol{C}^{-1}\boldsymbol{g}_j} \tag{11}$$

where $\boldsymbol{w}_{Capon,j}$ is the weight vector used for the adaptive beamforming method, and $\boldsymbol{g}_j$ the steering vector for grid point $\boldsymbol{\xi}_j$ as defined in Eq. 3. The source autopowers can be calculated in a similar way as in Eq. (5), using this time the weight vector above. In order to mitigate any potential ill-conditioning of $\boldsymbol{C}$, diagonal loading [25] is applied as

$$\boldsymbol{w}_{RAB,j} = \frac{\left(\boldsymbol{C} + \epsilon\mathbf{I}\right)^{-1}\boldsymbol{g}_j}{\boldsymbol{g}_j^* \left(\boldsymbol{C} + \epsilon\mathbf{I}\right)^{-1}\boldsymbol{g}_j} \tag{12}$$

where $\boldsymbol{I}$ is the $N \times N$ identity matrix. The value of the diagonal loading factor, ϵ, is usually determined empirically. One method proposed by Huang *et al.* [25] consists in calculating the maximum eigenvalue of the CSM and multiply it by a diagonal loading parameter, μ:

$$\epsilon = \mu \max\left[\mathrm{eig}\left(\boldsymbol{C}\right)\right] \tag{13}$$

where $\mathrm{eig}\left(\cdot\right)$ denotes the eigenvalues of a matrix. The value of μ is typically between 0.001 and 0.5 but needs to be iteratively determined considering a quality threshold in the difference between the obtained results and the CFDBF results, usually 3 dB. Therefore, one can start with an initial guess of $\mu = 0.001$ and increase it in each iteration until the results are satisfactory within the threshold. In general, smaller values of μ provide acoustic images with better array resolution but the computation can fail due to numerical instability. On the other hand, a larger value of μ generates results more similar to the CFDBF.

D. Functional Beamforming

Functional beamforming is based on the CFDBF algorithm. This technique was developed very recently (2014) by Dougherty [15, 16].

The CSM can be expressed as its eigenvalue decomposition:

$$\boldsymbol{C} = \boldsymbol{U}\boldsymbol{\Sigma}\boldsymbol{U}^* \tag{14}$$

where $\boldsymbol{U}$ is a unitary matrix whose columns are the eigenvectors $(\boldsymbol{u}_1, \ldots, \boldsymbol{u}_N)$ of $\boldsymbol{C}$ and $\boldsymbol{\Sigma}$ is a diagonal matrix whose diagonal elements are the eigenvalues $(\sigma_1, \ldots, \sigma_N)$ of $\boldsymbol{C}$.

The expression for the functional beamformer is

$$A_\nu(\boldsymbol{\xi}) = \left[\boldsymbol{w}^* \boldsymbol{C}^{\frac{1}{\nu}} \boldsymbol{w}\right]^\nu = \left[\boldsymbol{w}^* \boldsymbol{U}\boldsymbol{\Sigma}^{\frac{1}{\nu}} \boldsymbol{U}^* \boldsymbol{w}\right]^\nu \tag{15}$$

with ν a parameter which needs to be set by the user.

If a single sound source of strength s_k in the location $\boldsymbol{\xi}_k$ is considered, the dominant eigenvalue of $\boldsymbol{C}$ will be $\sigma_1 = s_k^2/2$ with the corresponding eigenvector $\boldsymbol{u}_1 = \boldsymbol{g}_k$. Recalling Eq. 10, the functional beamforming result for a general location $\boldsymbol{\xi}_m$ with steering vector $\boldsymbol{g}_m$ will now be

$$A_\nu(\boldsymbol{\xi}_m) = \left[\boldsymbol{w}_m^* \boldsymbol{C}^{\frac{1}{\nu}} \boldsymbol{w}_m\right]^\nu = \left[\frac{\boldsymbol{g}_m^* \left(\frac{s_k^2}{2} \boldsymbol{g}_k \boldsymbol{g}_k^*\right)^{\frac{1}{\nu}} \boldsymbol{g}_m}{\|\boldsymbol{g}_m\|^4}\right]^\nu = \frac{s_k^2}{2}\left[\frac{\boldsymbol{g}_m^* \boldsymbol{g}_k \boldsymbol{g}_k^* \boldsymbol{g}_m}{\|\boldsymbol{g}_m\|^4}\right]^\nu = \frac{s_k^2}{2}\left[\frac{\|\boldsymbol{g}_m^* \boldsymbol{g}_k\|^2}{\|\boldsymbol{g}_m\|^4}\right]^\nu \tag{16}$$

where it was used that $\boldsymbol{g}_k \boldsymbol{g}_k^*$ is an idempotent matrix, i.e. $(\boldsymbol{g}_k \boldsymbol{g}_k^*)^x = \boldsymbol{g}_k \boldsymbol{g}_k^*, \forall x \in \mathbb{R}$. It can be observed that the PSF factor is now powered to the exponent ν. As commented before, the PSF value is 1 in the correct source locations and alias points, and smaller than 1 everywhere else. Therefore, powering the PSF at a sidelobe will lower its level, leaving the true source value identical. For ideal conditions, the dynamic range for the functional beamforming should increase linearly with the exponent value, ν. For example, if a sidelobe level with the CFDBF was -10 dB compared to the main lobe value, and functional beamforming is employed with an exponent value of $\nu = 100$, the new sidelobe level would be -1000 dB. Thus, for an appropriate exponent value the dynamic range is significantly increased. The effect of the exponent is reduced for points near the true source, since the function $\cos^2 \phi$ is very close to 1 in that case. However, the beamforming peaks will be sharpened, improving the array resolution to some extent. The computational time for the functional beamforming is basically identical to the CFDBF one, since the only relevant operation added is the eigenvalue decomposition of $\boldsymbol{C}$, which is typically faster than the rest of steps involved in the beamforming process.

In previous work [15, 16] functional beamforming has been applied for numerical simulations, idealized cases with speakers as experimental noise sources and controlled experiments with components in a laboratory. To the best of the authors' knowledge, there is no literature dealing with the application of the functional beamforming algorithm for practical aeroacoustic experiments on full-scale aircraft during operational conditions. Therefore, this research is an attempt to provide an assessment of the method's performance for these cases.

III. Study with synthetic data

As a first step in assessing the performance of functional beamforming, this method is applied to synthetic data. The simulations were made using a 1.7 m diameter array with 32 microphones distributed along a spiral, similar to the one used for the experimental measurements, as shown in Fig. 1.

Typical values of the exponent ν are in the range of 20-300 [15], but as it will be discussed in subsection III A, using values larger than $\nu = 100$ did not improve significantly the results obtained in this research. Therefore, $\nu = 100$ will be used henceforth as a reference value in this paper. It can be easily verified that for $\nu = 1$ the CFDBF is obtained.

Figure 2 shows the results obtained with functional beamforming for a single 100 dB source situated at (0, 0) m and 1 m from the array emitting at 1000 Hz. A 100 dB range was selected for the source plots in order to appreciate the presence of sidelobes in a better way. Significant improvements of the dynamic range are observed when using a sufficiently high exponent value. The array spatial resolution is also improved, as it will be commented later in subsection III A. For the case of $\nu = 16$ there is already no visible presence of sidelobes. Increasing the exponent value further does not improve the results obtained, as observed here for the cases of $\nu = 64$ and $\nu = 300$, which are almost identical.

A larger dynamic range permits the detection of sources that would be masked by sidelobes and avoids the consideration of spurious sources as real sources, which is an issue for the CFDBF. Figure 3 illustrates this, where two sources are simulated: one 100 dB source at (0, 0) m and one 90 dB source at (0.875, 0.290) m, both emitting at 3000 Hz and 1 meter away from the array. The second source was intentionally situated in that position in order to place it under a sidelobe

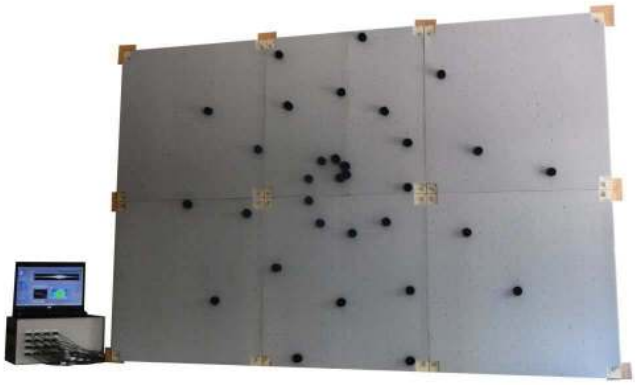

Fig. 1: Microphone distribution for the 32 microphone array used in the experimental measurements.

already present for the source at (0, 0) m when using CFDBF. As it can be observed, the second source cannot be properly identified in the CFDBF case, due to the abundance of high sidelobes of approximately the same SPL. On the other hand, functional beamforming succeeds in separating both sources clearly at the correct source locations and with the correct strengths.

A. Array spatial resolution improvement

In Fig. 2 it could be already noticed that the array resolution of the functional beamforming improves for increasing exponent values, ν. For a better view of this characteristic, in Fig. 4 the central cross sections for y=0 of the same beamforming source plots depicted in Fig. 2 are gathered. In this case a 10 dB range was selected in order to focus on the main lobe. It can be observed that the array resolution improves with increasing exponent values and that, once again, increasing the exponent value over a certain value does not improve the array resolution significantly any more.

This analysis was repeated for the case of a single point source emitting sound at different frequencies and for exponent values from 1 to 500, in order to investigate the variation of array resolution with frequency and exponent value. A square grid of 1000×1000 points was employed for this approach. Figure 5 illustrates the influence of ν on the array resolution for three different frequencies (1, 3 and 6 kHz). As it could be expected, higher frequencies have narrower lobes,

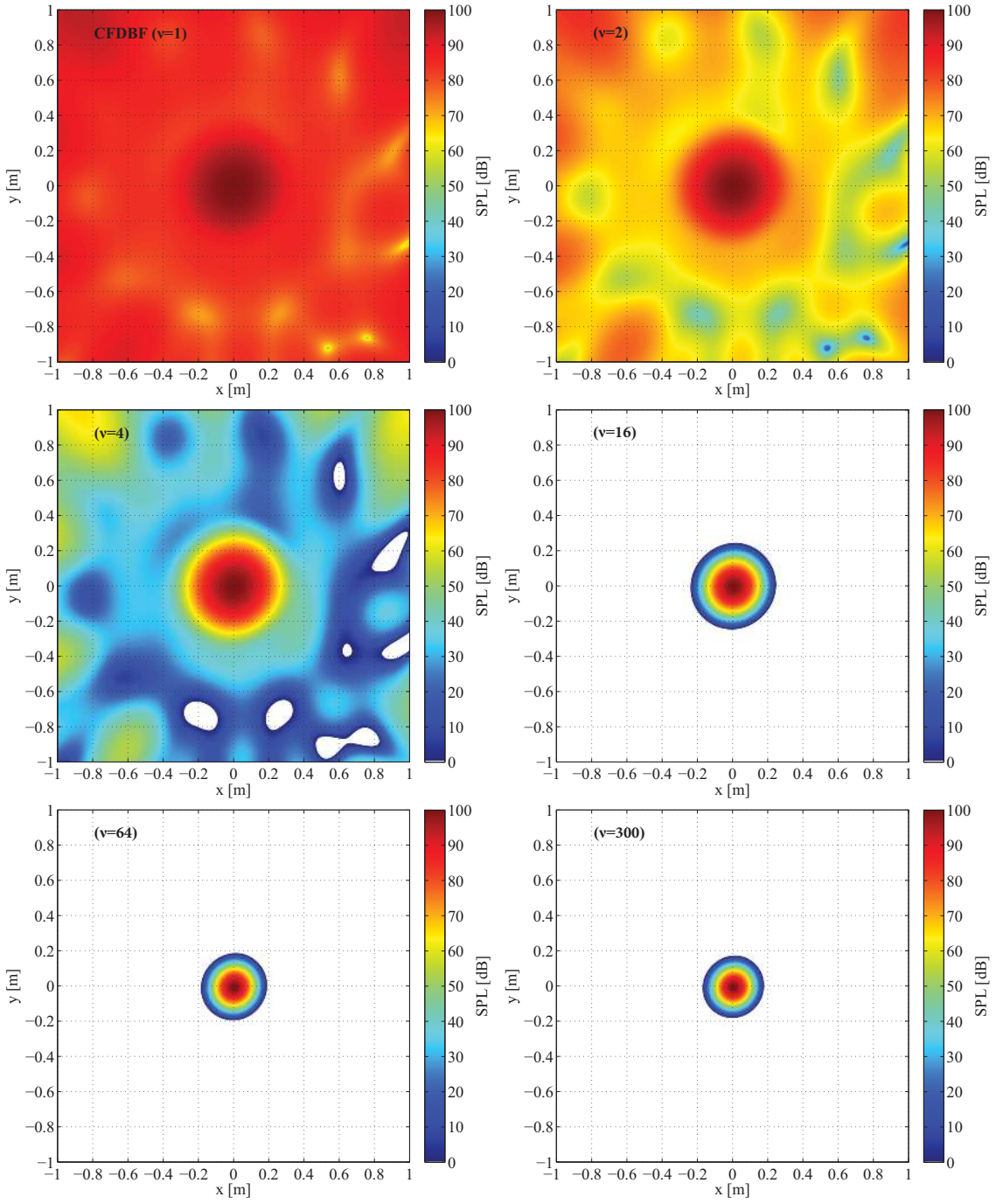

Fig. 2: Comparison between the obtained source plots for a single 100 dB source situated at (0, 0) m emitting at 1000 Hz and 1 m from the array, using form left to right and from top to bottom: CFDBF algorithm ($\nu = 1$) and functional beamforming algorithm for different exponent values: $\nu = 2$, $\nu = 4$, $\nu = 16$, $\nu = 64$ and $\nu = 300$.

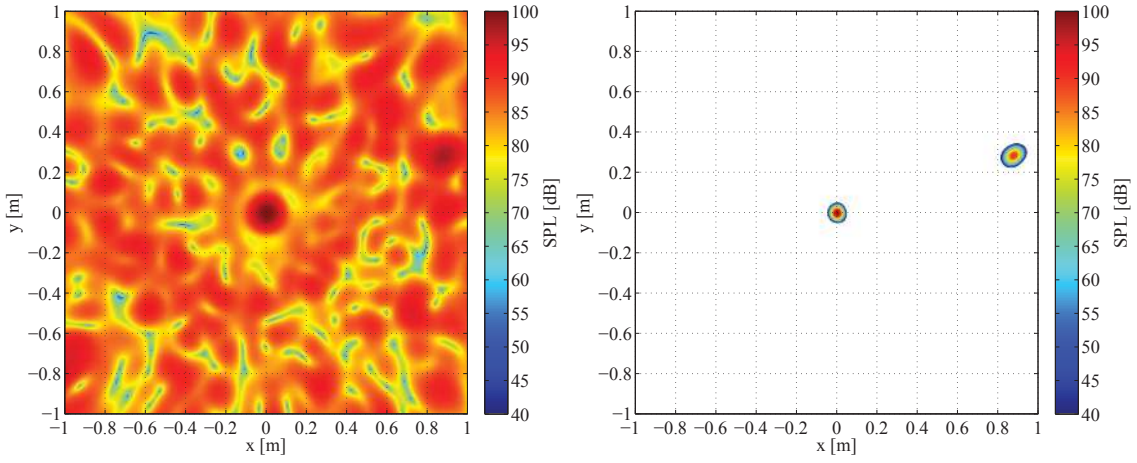

Fig. 3: Comparison between the results of the CFDBF (a) and functional beamforming with $\nu = 100$ (b) for two simulated sources: one 100 dB source at (0, 0) m and one 90 dB source at (0.875, 0.290) m both emitting at 3000 Hz 1 meter away from the array.

according to the Rayleigh criterion [28], which determines the minimum angular distance, φ, at which two different sources can still be distinguished as separated sources, using a circular aperture array:

$$\varphi = 1.220\frac{\lambda}{D} = 1.220\frac{c}{f\,D} \tag{17}$$

where φ is expressed in radians, λ is the wavelength considered and D is the diameter of the array, both in meters. According to Eq. (17), the minimum resolvable angular distance, φ, decreases linearly when increasing the frequency, as observed also in Fig. 5 (a). For the case studied in this analysis (1 source emitting at 1000 Hz situated 1 m away from an array with a 1.7 m effective diameter, as the one used for the experiments), taking $c = 340$ m/s, the Rayleigh criterion is $\varphi = 0.244$ rad. The minimum resolvable distance, R, in meters at a distance, h, of 1 m will, therefore be $R = h\tan\varphi \approx 0.25$ m. This value is slightly smaller than the one obtained in the simulations, 0.30 m, due to the limited number of microphones considered (32) and the fact that the microphone array considered is not strictly circular.

It can be observed in Fig. 5 that the beamwidth decreases rapidly with increasing ν. However,

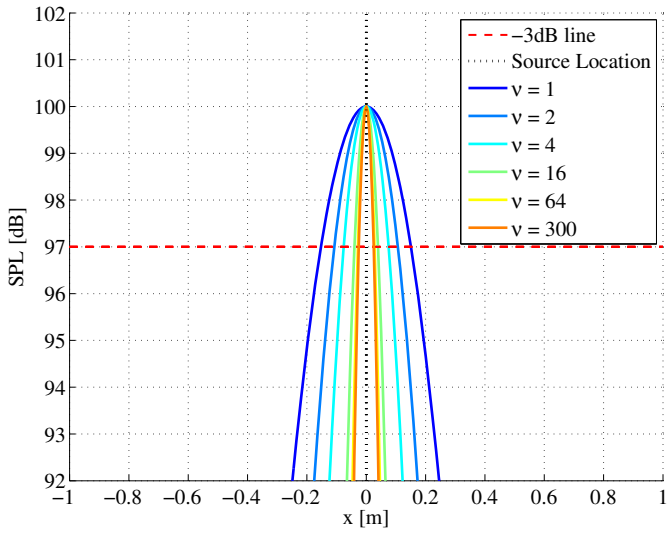

Fig. 4: Comparison between the cross sections of the beamforming source plots at y=0 for a single 100 dB source situated at (0, 0) m emitting at 1000 Hz and 1 m from the array, using CFDBF algorithm ($\nu = 1$) and functional beamforming algorithm for different exponent values: $\nu = 2$, $\nu = 4$, $\nu = 16$, $\nu = 64$ and $\nu = 300$.

after a threshold value it remains approximately constant. In Fig. 5 (b) it can be noticed that the three cases approach an asymptotic value of relative width of the main beam of around 20% of the ones obtained with the CFDBF algorithm ($\nu = 1$). In general, values higher than $\nu = 100$ barely improve the array resolution. However, notice that even if the array spatial resolution is improved with the functional beamforming, two hypothetical sources emitting at the same frequency placed closer than the minimum resolvable distance according to the Rayleigh criterion, would still not be identified as different sources by functional beamforming.

B. SPL reduction for the Functional Beamforming

In Eq. (16), $A_\nu(\boldsymbol{\xi}_m)$ is monotonically decreasing as the exponent ν increases (except for the case that all the eigenvalues of $\boldsymbol{\Sigma}$ are equal [15]). In practice, the position vectors for the considered grid may not exactly coincide with the actual position vector of the source. In that case, the PSF factor between the actual source steering vector $\boldsymbol{w}_k$ and the closest grid point to the source steering vector $\boldsymbol{w}_m$ is now (according to Eq. (16) and considering small values of ϕ):

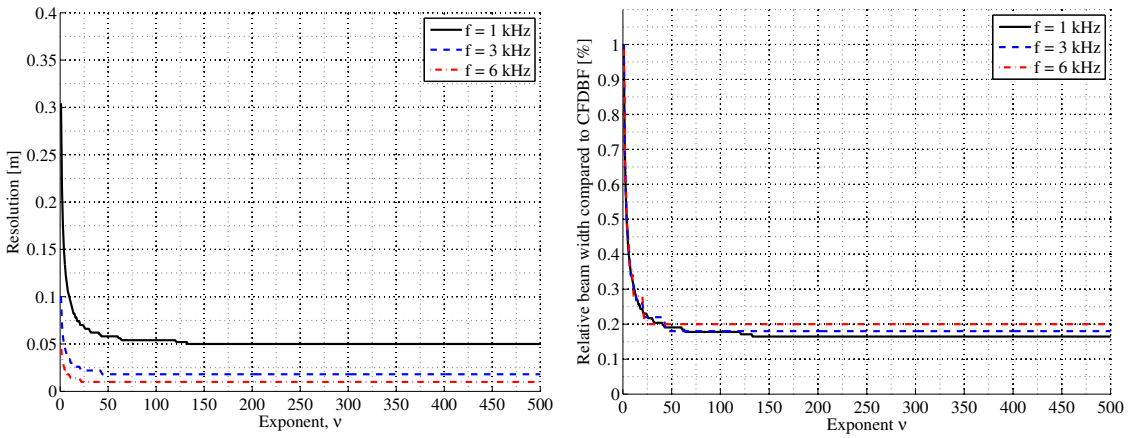

(a) (b)

Fig. 5: Array resolution for functional beamforming for different exponent ν values and different frequencies: 1, 3 and 6 kHz . (a) Absolute width of the main beam in meters for a single 100 dB source 1 m away from the microphone array. (b) Widths of the main beam for the same cases compared to the ones obtained with the CFDBF algorithm ($\nu = 1$).

$$\|\boldsymbol{w}_m^* \boldsymbol{w}_k\|^{2\nu} \approx \cos^{2\nu}\phi \approx \left(1 - \frac{\phi^2}{2}\right)^{2\nu} \tag{18}$$

Bernoulli's inequality provides

$$\cos^{2\nu}\phi \approx \left(1 - \frac{\phi^2}{2}\right)^{2\nu} \geq 1 - \nu\phi^2 \tag{19}$$

Therefore, any potential difference between the source position $\boldsymbol{\xi}_k$ and the closest grid point $\boldsymbol{\xi}_m$ would then imply a SPL reduction given by the factor $\left(1 - \nu\phi^2\right)$. Therefore, finer grids and accurate array calibration are preferred, since they imply lower values of ϕ, with the limitation of their higher computational demand.

In case significant SPL reductions are observed, the value of the main lobe provided by the CFDBF method should be taken as a reference. A solution for this issue is to use maximum SPL with the CFDBF method, which is assumed to provide the correct value. This approach was employed in this paper in order to evaluate the correct SPL values.

C. Comparison of Functional Beamforming with other imaging methods

In order to assess the expected performance of the different beamforming algorithms selected, several simulations were performed using the same scan grids, locations and estimated noise sources present in the experimental data from the fly-overs considered in subsection V A. It should be noticed that in this research for the CLEAN methods, the loop gain [20] was selected to be 1 and that the width of their clean beams was increased 5 times in order to be able to appreciate them visually in the picture.

The first case corresponds to a single 136 dB source emitting at 1629 Hz which would model the nose landing gear noise from an Airbus A321 (as illustrated later in Fig. 12). In Fig. 6 the source maps for five different beamforming algorithms are presented in order to assess their performance. A 60 dB range was chosen, in order to show possible sidelobes. In this case, the RAB diagonal loading parameter, μ, was determined iteratively to be 0.0005 (according to the criterion explained in subsection II C), resulting in a value of $7.6 \cdot 10^{-8}$ for ϵ.

From Fig. 6, it can be noticed that the functional beamforming with $\nu = 100$ improves both the dynamic range (about 23 times larger) and array spatial resolution with respect to the CFDBF. The CLEAN-PSF improves the dynamic range to a lower extent and improves the array spatial resolution even more than the functional beamforming. However, this is artificial, since the main lobe is now a synthetic clean beam introduced by the user as a point source. The same fact happens for the CLEAN-SC case, but now the dynamic range is improved in a similar way as in the functional beamforming case. Finally, the RAB technique also provides a dynamic range and array spatial resolution improvements comparable to the ones obtained by the CLEAN-SC method. For this case, the functional beamforming, CLEAN-SC and RAB methods provide a very large dynamic range. The array spatial resolution offered by the functional beamforming is comparably better than the one from CFDBF, but is improved even further by the CLEAN-SC and RAB methods.

The second case corresponds to two 124 dB sources emitting at 7138 Hz which would model the main landing gear noise from a Fokker 70 (as illustrated later in Fig. 13). The wheels of the main landing gear of a Fokker 70 [29] are separated a distance of approximately 5 m, which is larger than the 2 m Rayleigh criterion distance for this case (using Eq. (17) with $f = 7138$ Hz

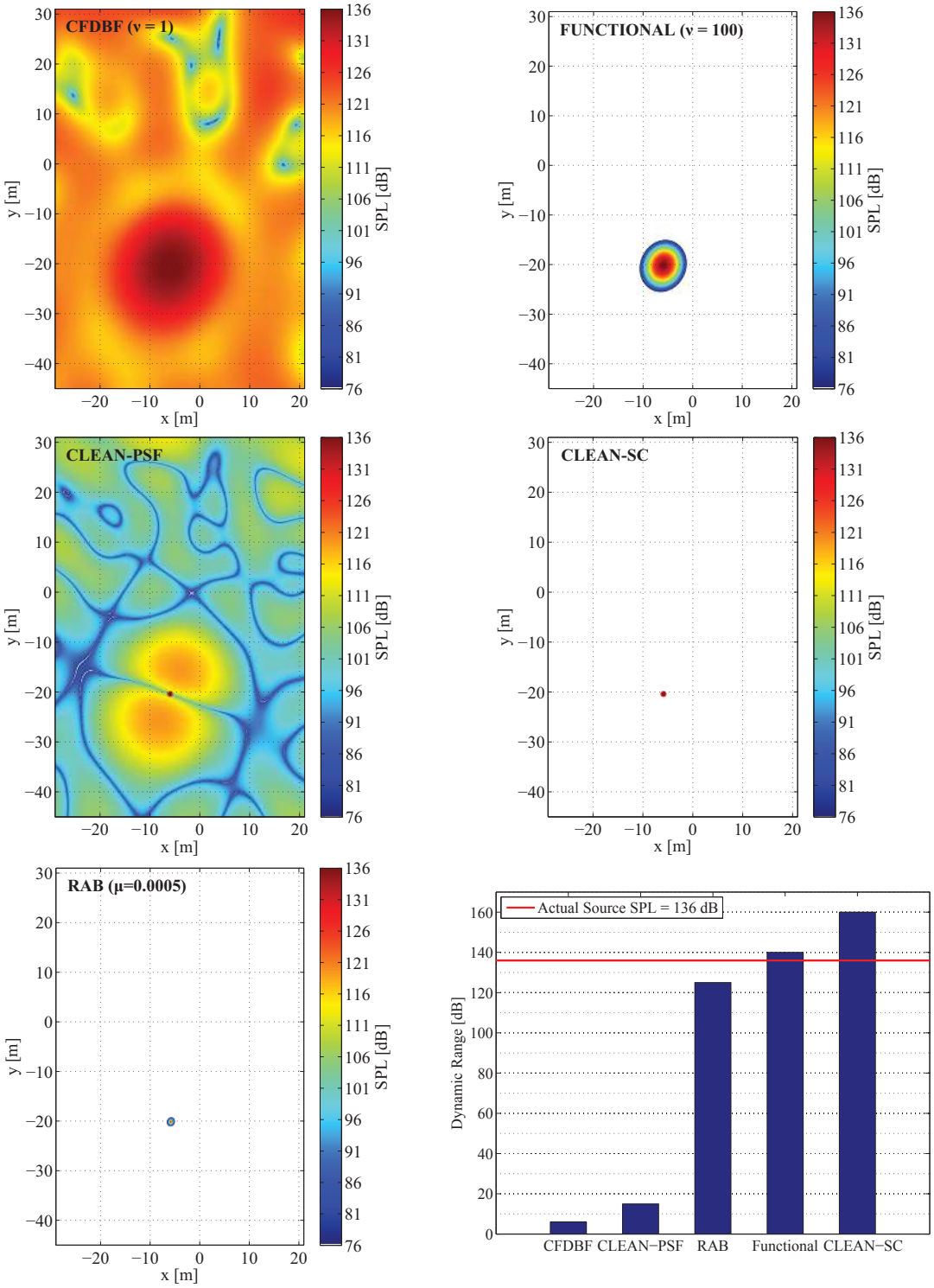

Fig. 6: Comparison between the beamforming source plots for a simulated 136 dB source emitting at 1629 Hz employing different algorithms. From left to right and from top to bottom: CFDBF, Functional beamforming with $\nu = 100$, CLEAN-PSF, CLEAN-SC, RAB with a diagonal loading parameter of $\mu = 0.0005$ and the dynamic range for each method for this case.

and $h = 61$ m, as explained in subsection III A). Therefore, it should not be a problem to identify both wheels as separate sound sources. In Fig. 7 the source maps for the same five beamforming algorithms employed before are presented. A 12 dB range was selected for clarity reasons in this case, since higher frequencies present a higher amount of sidelobes with higher levels. The RAB diagonal loading parameter, μ, was determined to be 0.08 and the value of the diagonal loading factor, ϵ, $2.9 \cdot 10^{-5}$.

From Fig. 7, it can be observed that, once again, the functional beamforming considerably improves both the dynamic range and array spatial resolution with respect to the CFDBF results. The CLEAN-PSF behaves as previously, increasing the dynamic range to some extent. However, the CLEAN-SC method now fails to identify both sources, localizing only the sound source located on the right. This is the main drawback of the CLEAN-SC algorithm. Since it is based on the spatial coherence between sidelobes and the main lobe, it cannot separate two different sources emitting at the same frequency. The RAB technique also improves the dynamic range and array spatial resolution, but in this case to a much lower extent than the functional beamforming. The absolute values of the dynamic ranges for all the methods, except for the CLEAN-SC, are considerably reduced for this case with two sources and high frequency sound compared to the case of one source emitting at lower frequency.

The source position and SPL values provided by all methods are in perfect agreement with the "true" values used for creating the synthetic data. The only method which does not provide the correct SPL value immediately is the RAB, since its diagonal loading parameter, μ, has to be adjusted manually to provide comparable results as the CFDBF. For the functional beamforming case, a sufficiently fine grid needs to be employed in order not to discard actual sound sources and provide correct SPL values when using large exponents.

IV. Experimental set-up

In order to obtain a representative amount of data, 115 fly-over measurements were recorded at Schiphol airport using a 32 microphone array in a spiral distribution, see Fig. 1. This array configuration was chosen due to its varying element spacing, which provides good results over a wide range of frequencies with a small amount of sidelobes [30]. The array has an effective diameter

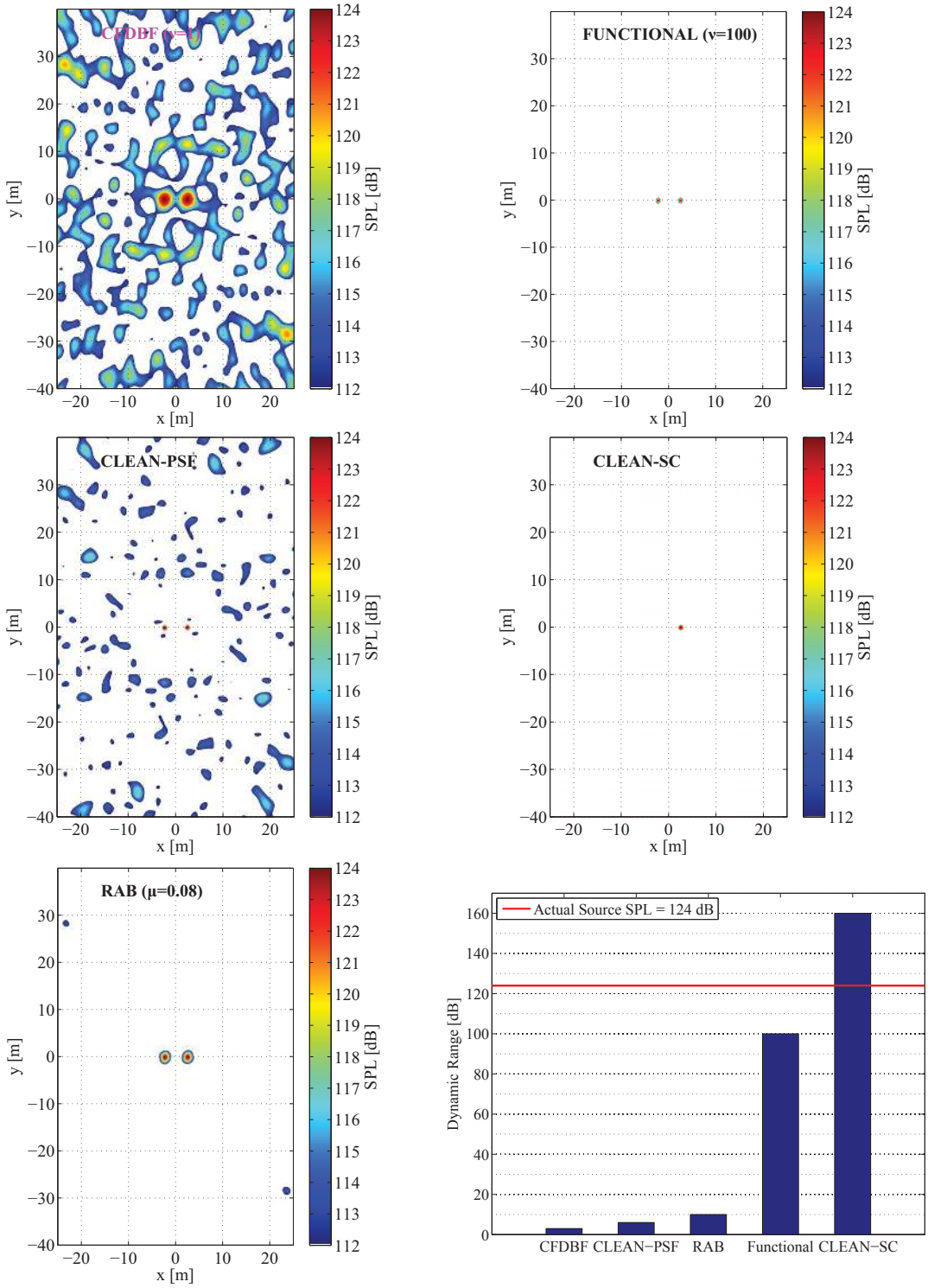

Fig. 7: Comparison between the beamforming source plots for two simulated 124 dB sources emitting at 7138 Hz employing different algorithms. From left to right and from top to bottom: CFDBF, Functional beamforming with $\nu = 100$, CLEAN-PSF, CLEAN-SC, RAB with a diagonal loading parameter of $\mu = 0.08$ and the dynamic range for each method for this case.

of 1.7 m and uses band filters for the frequency range from 45 Hz to 11,200 Hz. The sampling frequency employed was 40 kHz.

The flight trajectory during the landing approach is typically less variable than the one for take-off, since all aircraft follow the Instrument Landing System (ILS) approach. Moreover, the main reason for recording landing aircraft is because the engines are usually at approach idle, so engine noise is less dominant and thus other noise sources, such as airframe noise, are more likely to be identified. Hence, the microphone array was placed 1,240 m to the South of the threshold of the Aalsmeerbaan Schiphol airport runway (36R), used for landing, as illustrated in Fig. 8. Henceforth, the data will be referred to the distances to the array, with the Y-axis in the direction of the runway and the X axis perpendicular to it. The measurements were taken on two different days with similar weather conditions and low wind speeds. The recorded data correspond to 21 different aircraft types gathered in 12 different aircraft families, from which the Boeing 737 is the most numerous with 59 measurements available.

Fig. 8: Experimental set-up located 1,240 m to the South of the threshold of the Aalsmeerbaan (36R) Schiphol airport runway.

The flight paths of the aircraft have to be precisely estimated and recorded together with a reference time signal that can later be used for the synchronisation with the acoustic data. The trajectories need to be determined in order to properly take into account the propagation, moving source and Doppler effects. Three different methods were employed for calculating the aircraft position and velocity, each of them using data from a different source:

- ADS-B (Automatic Dependent Surveillance-Broadcast): Aircraft determine their own position and attitude using the Global Navigation Satellite System (GNSS) in combination with the on-board Inertial Navigation System (INS). For surveillance purposes, this information is actively sent to the ground approximately twice per second. However, the ADS-B is a rather new system and not all the aircraft are currently equipped with this transponder. In this research, only 59 out of the 115 recorded fly-overs had this information.

- Ground radar: Air Traffic Control uses position, altitude and identity data from the ground radar for aircraft surveillance in the departure and approach phases. Nowadays all commercial aircraft are equipped with a Mode C transponder to reply this information. However, the aircraft position is only detected every 4 seconds due to the rotation time of the radar. Furthermore, there is a minimum height (around 65 m) below which no position data is recorded by the radar, but since the approach is expected to be a straight line, for this research the final part of the trajectories is linearly extrapolated using the least squares method applied to the last 11 data points.

- Extrapolation of optical camera images: An optical camera is integrated in the microphone array at a fixed angle facing straight up from the ground. When the aircraft comes overhead, it flies through the camera's field of view, as depicted in Fig. 12. The recordings from the optical camera are used to determine the aircraft height and ground speed when above the array, which can be extrapolated to estimate its full trajectory during the fly-over.

All three methods were used and were found to provide very similar results. The extrapolation of the optical camera images is preferred due to its versatility and availability and because it is easier to overlay the beamforming results on to the optical frames (this is included in the color version of this paper, while an outline of each aircraft was added in the black and white version). The average flight height and average aircraft velocity were determined to be 67 m and 271 km/h, respectively. The estimated overhead time was confirmed by checking the Doppler shifted lines in the spectrograms.

V. Experimental results

In order to assess the performance of the functional beamforming algorithm with experimental data, the 115 recorded fly-over measurements were processed with the same five beamforming methods employed previously in the simulations. The SPL values for the functional beamforming have already been corrected according to the considerations explained in subsection III B.

As a first step it is investigated, if $\nu = 100$ is also appropriate for the experimental data. Figure 9 shows acoustic images for a fly-over of a Boeing 744, for a low frequency of 400 Hz and for exponent values ν of 1, 16, 64 and 100. It can be observed that higher exponent values cause the main lobe to become remarkably narrower, i.e. improving the array spatial resolution as expected. No major improvements are observed for the results with $\nu = 64$ and $\nu = 100$. The figure now clearly shows that the noise source at that frequency is situated close to the main landing gear.

In Fig. 10 the variation of the array resolution is shown with the exponent value, ν, from 1 to 500, but now using a A321 fly-over and a frequency of 1629 Hz. For comparison, in the figure also results of simulations (similar to figure 5 but now for a frequency of 1629 Hz) are shown. The behavior for simulated and experimental data is in good agreement.

For the remainder of the analysis, out of the 115 results, two have been selected for a more detailed study as presented below. However, in general, these examples are representative for all fly-overs. In the following subsections the results for the experimental cases analogous to the simulated ones in section III are presented and discussed.

A. Comparison of Functional Beamforming with other imaging methods

The frequency spectra at the overhead time for two different fly-overs measurements are presented in Fig. 11, showing one clear interesting peak in each spectrum: at 1629 Hz for the case of an Airbus A321 and at 7138 Hz for a Fokker 70. In Figs. 12 and 13 the corresponding acoustic images for these two examples are presented.

The results for the fly-over of the Airbus A321 are gathered in Fig. 12 where a 60 dB range was selected again (resembling Fig. 6), in order to show possible sidelobes. The aircraft outline has been manually added to the pictures for clarity reasons. After the beamforming process for the 1629 Hz peak, the noise was determined to come from the nose landing gear. The CFDBF

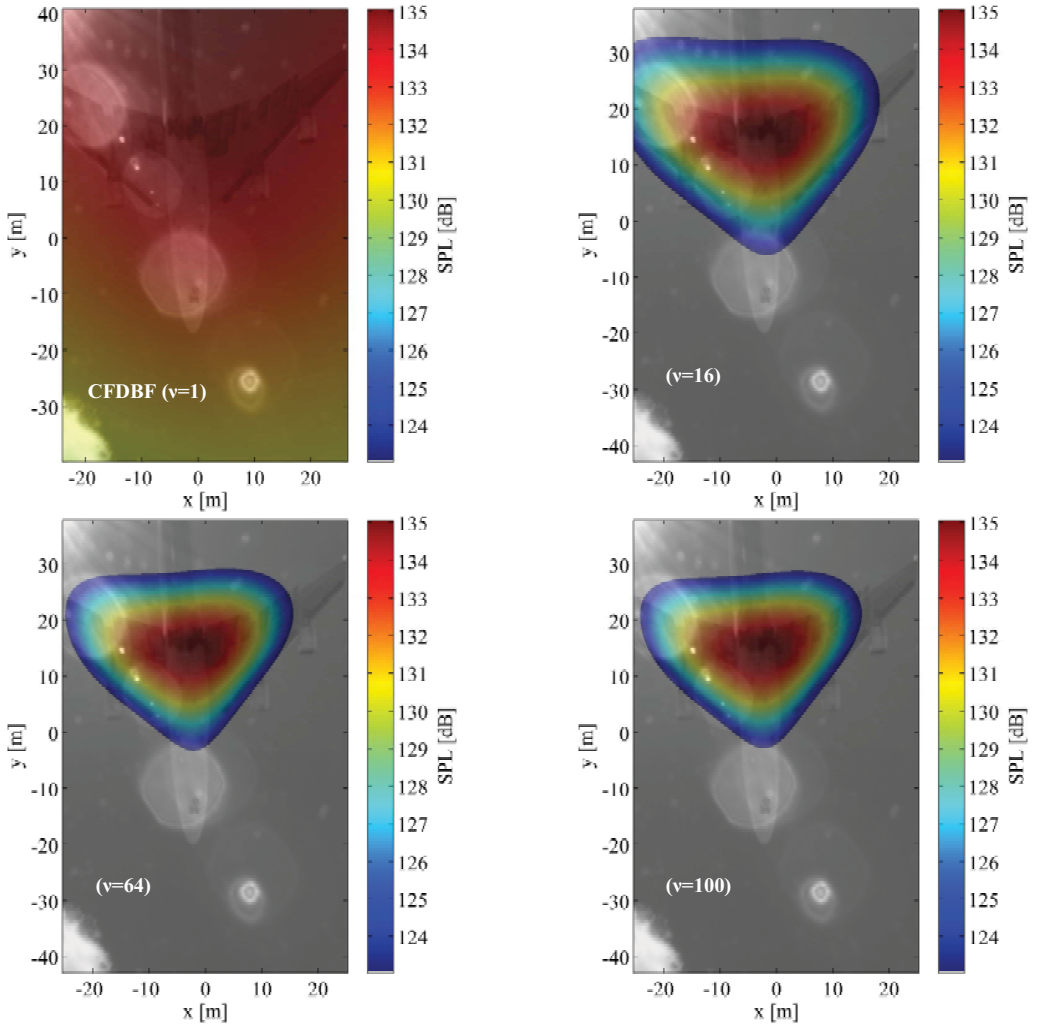

Fig. 9: Comparison between the array spatial resolution of the main lobe for a Boeing 744 fly-over at 400 Hz. From left to right and from top to bottom: CFDBF ($\nu = 1$) and functional beamforming for different exponent values: $\nu = 16$, $\nu = 64$ and $\nu = 100$.

source plot shows a wide main lobe coming approximately from the nose landing gear, but is greatly contaminated with sidelobes, hampering the noise sources identification. When using functional beamforming with an exponent value of $\nu = 100$, the sidelobes virtually disappear and the array spatial resolution is improved by approximately a factor 6, similar to the simulations. The CLEAN-PSF method improves to some extent the CFDBF results and identifies the source location, but the source map still presents several sidelobes of lower level which could still be confused with real sources. As it happened in subsection III C, the CLEAN-SC algorithm manages to overcome this issue and achieves the localization of the noise source with an array spatial resolution selected by

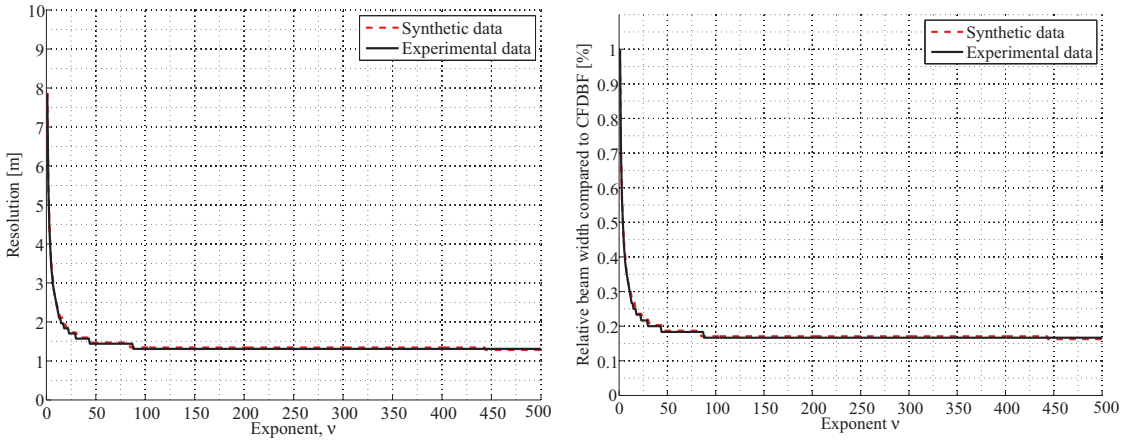

(a) (b)

Fig. 10: Array spatial resolution for functional beamforming as a function of exponent ν for simulated and experimental data for the single 1629 Hz source case. (a) Absolute width of the main beam in meters. (b) Widths of the main beam compared to the ones obtained with the CFDBF algorithm ($\nu = 1$).

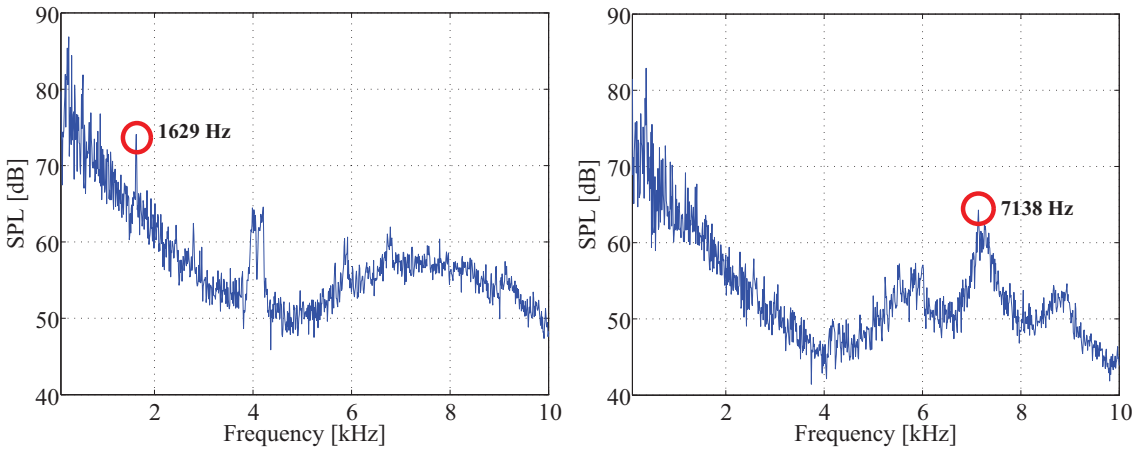

(a) (b)

Fig. 11: Frequency spectra during the time overhead (using a 0.1 s time window) for the experimental measurements considered: (a) Airbus A321. (b) Fokker 70.

the user. For the RAB method the diagonal loading parameter, μ, needs to be carefully selected due to the sensitivity of the method. An iterative process was performed. An appropriate value for μ was found to be 0.005, which is one order of magnitude larger than required in the analogous

case with synthetic data. This method does not offer such successful results as in Fig. 6, but still provides an improved source plot compared to the CFDBF one. In general, the dynamic ranges for the experimental data are similar to those obtained with the simulations. The experimental values are slightly lower due to background noise and experimental errors. Only the RAB method has a dynamic range more than 3 times smaller for the experimental case.

For the Fokker 70, the beamforming results are gathered in Fig. 13 where a 12 dB range was chosen again, for the same reasons as in Fig. 7. Observing Fig. 13 (a) it seems that the noise comes from two sources located close to the main landing gear, but the CFDBF presents so many sidelobes that it is difficult to confirm this fact. Functional beamforming solves this problem, eliminating basically all the sidelobes for this dB range and improving again the array spatial resolution. The CLEAN-PSF method achieves the identification of the two sources from the main landing gear, but the source map still presents several strong sidelobes which could be again confused with real sources. The CLEAN-SC algorithm is unable to identify two different sources at the same frequency. In this case, the RAB method required a diagonal loading parameter, $\mu = 0.1$, which is once again one order of magnitude larger than required in the case with synthetic data. This value of μ is also 2 orders of magnitude larger than for the 1629 Hz case due to the higher frequency, but it offers results comparable to the simulated ones. With respect to the dynamic range of each method, it is generally lower than for the low frequency case considered before, due to the higher number of sidelobes at higher frequencies.

B. Computational time

The computational times required for each of the methods employed in this research are now calculated for the same case (beamforming for a single frequency using a 2000 $\times$ 2000 grid) and compared in Fig. 14. All the computations in this research were performed using an Intel Xeon CPU 3.7 GHz with 8 GB of RAM. As it could be expected, the CFDBF method is the fastest one and the rest of the methods spend longer times, since they are based on the CFDBF algorithm and require additional operations. However, the functional beamforming algorithm requires only approximately 30% more time than the CFDBF, since the only additional operation required is a spectral decomposition, while the CLEAN methods spend approximately 330% more time, since

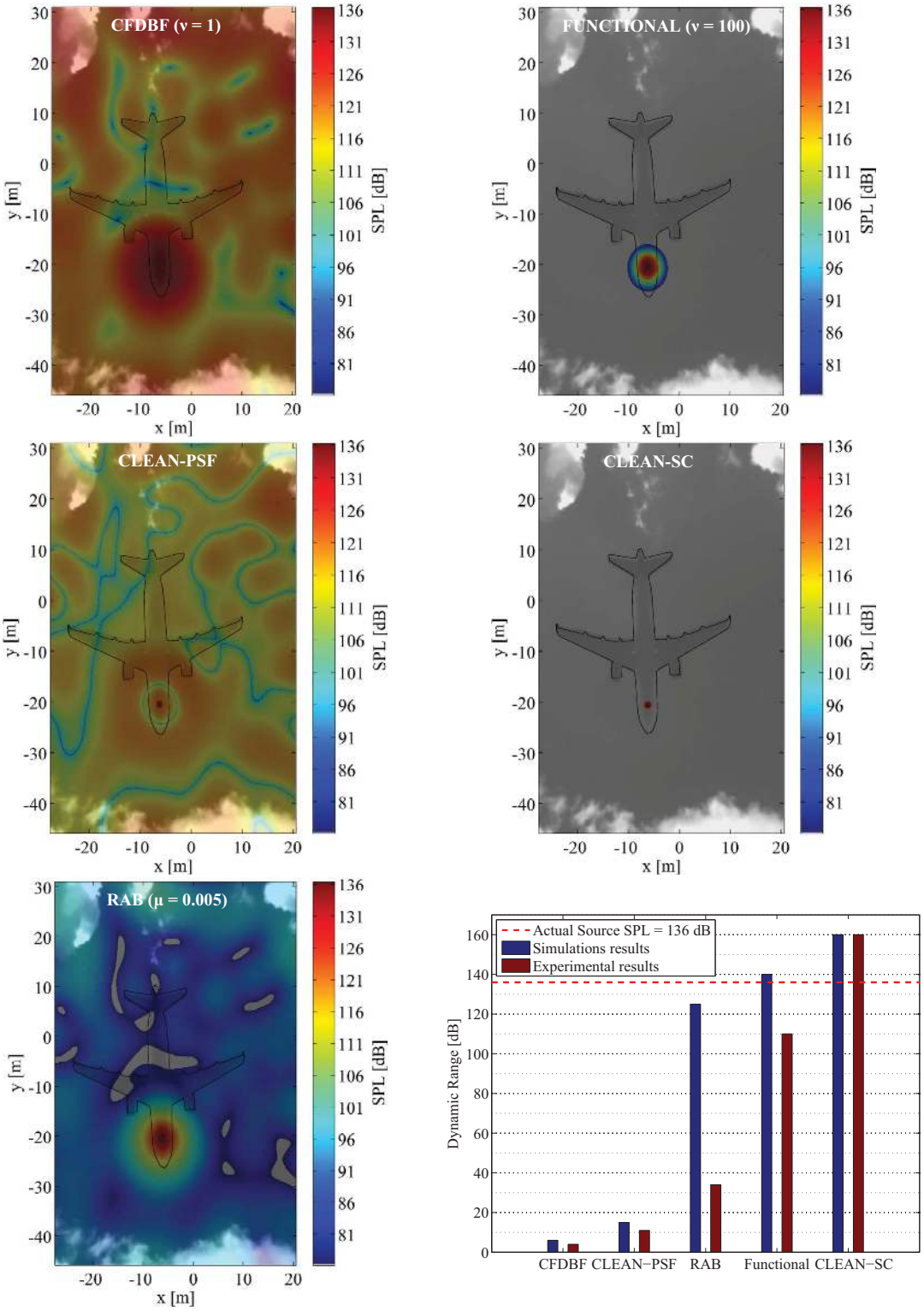

Fig. 12: Comparison between the beamforming source plots for an Airbus A321 fly-over at 1629 Hz employing different algorithms. From left to right and from top to bottom: CFDBF ($\nu = 1$), Functional beamforming with $\nu = 100$, CLEAN-PSF, CLEAN-SC, RAB with a diagonal loading parameter of $\mu = 0.005$ and the comparison between the dynamic range obtained for the simulated and experimental data.

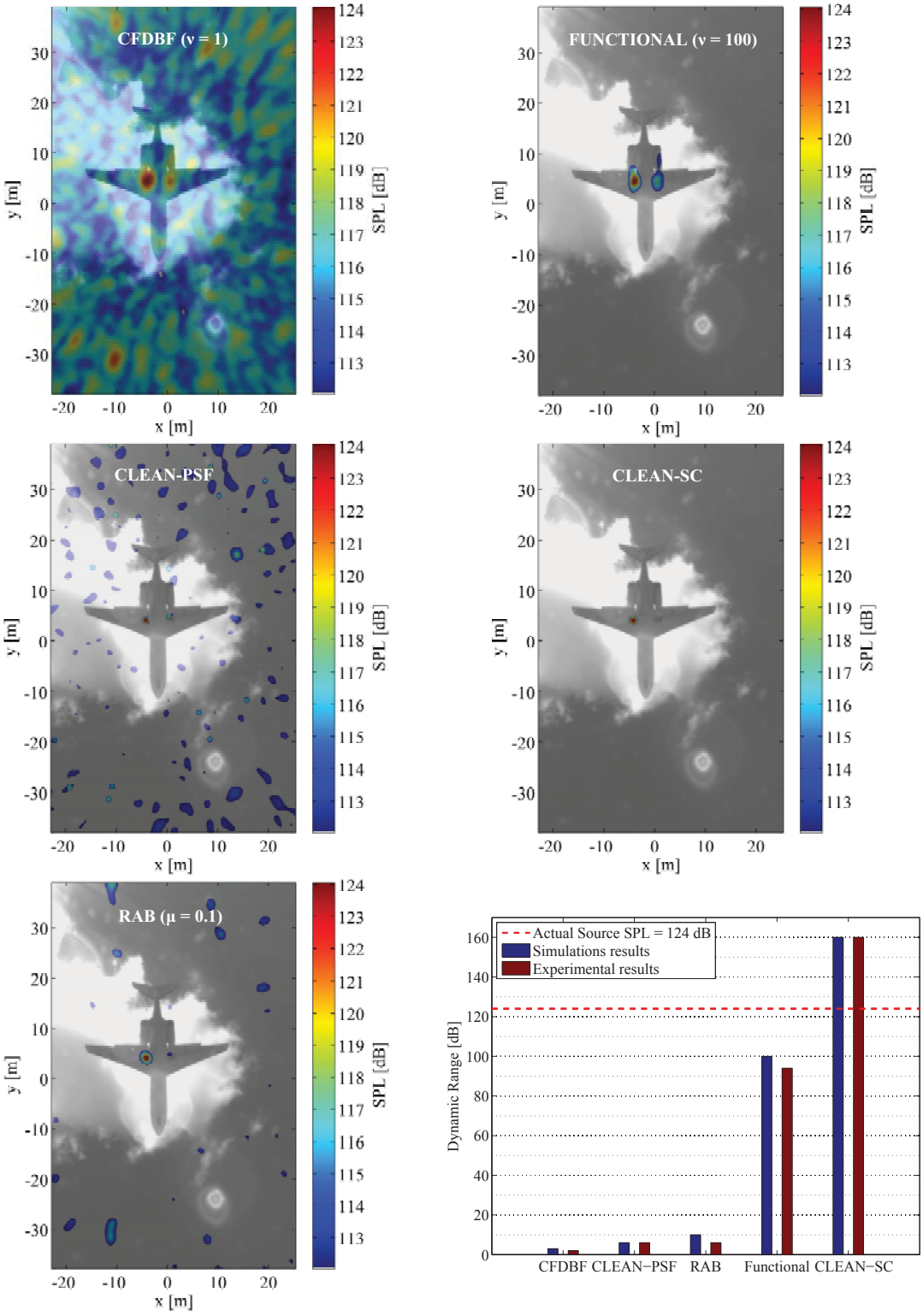

Fig. 13: Comparison between the beamforming source plots for a Fokker 70 fly-over at 7138 Hz employing different algorithms. From left to right and from top to bottom:CFDBF ($\nu = 1$), Functional beamforming with $\nu = 100$, CLEAN-PSF, CLEAN-SC, RAB with a diagonal loading parameter of $\mu = 0.1$ and the comparison between the dynamic range obtained for the simulated and experimental data.

they deconvolve the CFDBF source map. The RAB method is somehow between those two values, employing over 200% more time than the conventional beamforming, due to the inverse matrix calculations involved.

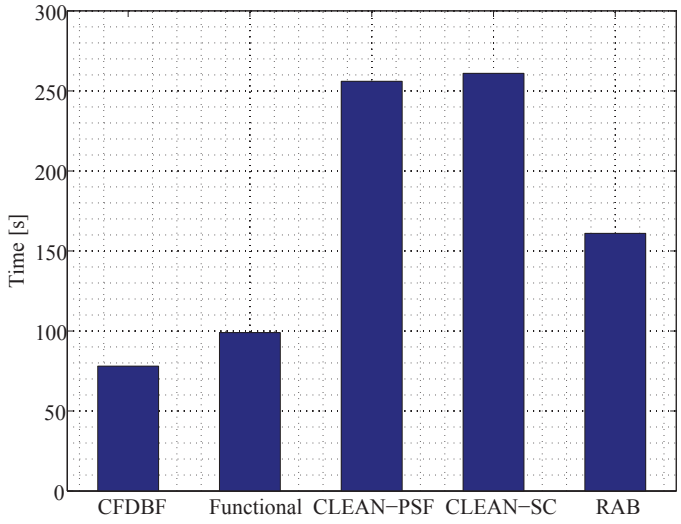

Fig. 14: Computational times required for a beamforming operation of a single frequency in a grid of 2000 × 2000 grid points.

VI. Conclusions

In this paper the functional beamforming algorithm was employed for the first time in full-scale field experiments with fly-over measurements of aircraft. Its performance was assessed and compared to other beamforming methods, in this case CFDBF, CLEAN-PSF, CLEAN-SC and RAB.

The expected performance of all the mentioned methods was simulated using synthetic data which attempted to model real aeroacoustic sources similar to the ones identified in the experimental measurements. The experimental and simulated results agree in a very satisfactory way. The following points describe the performance of each method, with a special emphasis on their dynamic range and array spatial resolution. These aspects are highly important when considering full scale fly-over measurements, as the distance between the array and the aircraft is at least few tens of meters and the aim is to identify all the sound sources on the aircraft.

- The functional beamforming algorithm is a promising alternative for the CFDBF method as the standard beamforming algorithm used in aeroacoustics, since it provides considerably

higher dynamic range (around 30 to 40 times larger) and an array spatial resolution approximately a factor 6 better than the CFDBF, requiring a similar computational time. Unlike the CLEAN-SC method, it can identify several sources emitting at the same frequency and render continuous distributed sound sources. Its main drawback, the SPL reduction for high values of the exponent parameter ν can be easily corrected for (as explained in subsection III B).

- The CLEAN-PSF method improves to some extent the CFDBF results, especially concerning the array spatial resolution. However, it is more computationally expensive.

- The CLEAN-SC method, on the other hand, offers even better array spatial resolution and dynamic range than the functional beamforming. However, its main drawback is that it is not able to separate two sources emitting at the same frequency, due to the spatial coherence hypothesis it is based on. As a deconvolution method, the required computational time is also larger.

- Finally, the RAB method works well with synthetic data, but is very sensitive to perturbations and experimental errors. The diagonal loading parameter, μ, needs to be carefully selected for each case and frequency. This technique can easily become unstable and it presents the largest differences between the synthetic and the experimental results.

The sources analyzed in this paper are airframe noise sources, particularly the landing gear noise, which are dominant for certain aircraft types during landing for certain frequencies. These sound sources might be overlooked by the CFDBF method, but are clearly detected by the functional beamforming technique.

References

[1] Lighthill, M. J., "On sound generated aerodynamically, I. General theory," Proceedings of the Royal Society of London. Series A, Mathematical and Physical Sciences. 221, pp 564-587. 1952.

[2] Simons, D. G., Snellen, M., Midden, B., Arntzen, M. and Bergmans D. H. T., "Assessment of noise level variations of aircraft fly-overs using acoustic arrays," Journal of Aircraft, Vol. 52, No. 5, pp 1625-1633. September-October 2015.

[3] Sijtsma, P., "Phased array beamforming applied to wind tunnel and fly-over tests," National Aerospace Laboratory (NLR), NLR-TP-2010-549. December 2010.

[4] Liu, Y., Quayle, A., Dowling, A. P. and Sijstma, P., "Beamfoming correction for dipole measurement using two-dimensional microphone arrays," Journal of the Acoustical Society of America, No. 124, pp 182-191. 2008.

[5] Camier, C., Padois, T., Provencher, J., Gauthier, P. A., Berry, A., Blais, J. F., Patenaude-Dufour, M. and Lapointe, R., "Fly-over source localization on civil aircraft," AIAA Paper 2013-2261. May 2013.

[6] Dougherty, R. P., Ramachandran, R. C. and Raman, G., "Deconvolution of Sources in Aeroacoustic Images from Phased Microphone Arrays Using Linear Programming," AIAA Paper 2013-2210. May 2013.

[7] Herold, G. and Sarradj, E., "Preliminary benchmarking of microphone array methods," Berlin Beamforming Conference, BeBeC 2014-10, 2014.

[8] Ishii, Y., Hald, J., Ishii, T., Oinuma, H., Nagai, K., Yokokawa, Y. and Yamamoto, K., "High-resolution fly-over beamforming using a practical array," Berlin Beamforming Conference, BeBeC 2014-16, 2014.

[9] Sijtsma, P. and Stoker, R. W., "Determination of Absolute Contributions of Aircraft Noise Components using Fly-Over Array Measurements," AIAA Paper 2004-2958. 2004.

[10] Sijtsma, P. and van der Wal, H. M. M., "Identification of Noise Sources on Civil Aircraft in Approach using a Phased Array of Microphones," National Aerospace Laboratory (NLR), NLR-TP-2004-166. April 2004.

[11] Siller, H. A., "Localisation of sound sources on aircraft in flight," Berlin Beamforming Conference, BeBeC 2012-01, 2012.

[12] Michel, U., Barsikow, B., Helbig, J., Hellmig, M. and Schüttpelz, M., "Flyover noise measurements on landing aircraft with a microphone array," AIAA Paper 1998-2336. 1998.

[13] Ruijgrok, G. J. J., *Elements of aviation acoustics.* Second edition 2007. VSSD. Delft, The Netherlands. ISBN-10 90-6562-155-5.

[14] Howell, G. P., Bradley, A. J., McCormick M. A. and Brown J. D., "De-Dopplerization and acoustic imaging of aircraft flyover noise measurements," Journal of Sound and Vibration, No. 105, pp 151-167. 1986.

[15] Dougherty, R. P., "Functional Beamforming," Berlin Beamforming Conference, BeBeC 2014-01, 2014.

[16] Dougherty, R. P., "Functional Beamforming for Aeroacoustic Source Distributions," AIAA Paper 2014-3066, June 2014.

[17] Sijtsma, P., "Experimental techniques for identification and characterisation of noise sources," National

Aerospace Laboratory (NLR), NLR-TP-2004-165. April 2004.

[18] Mueller, T. J. (Ed.), *Aeroacoustic Measurements*. First edition 2002. Springer-Verlag Berlin Heidelberg. ISBN-978-3-642-07514-8.

[19] Hogbom J. A., "Aperture Synthesis with a Non-Regular Distribution of Interferometer Baselines," Astronomy and Astrophysics Supplement Series. No. 15, pp 417-426. 1974.

[20] Sijstma, P., "CLEAN based on spatial source coherence," AIAA Paper 2007-3436, 2007, (also National Aerospace Laboratory (NLR), NLR-TP-2007-345. December 2007).

[21] Brooks, T. F. and Humphreys, W. M., "A Deconvolution Approach for the Mapping of Acoustic Sources (DAMAS) determined from phased microphone arrays," AIAA Paper 2004-2954, 2004.

[22] Brooks, T. F. and Humphreys, W. M., "Three-Dimensional Application of DAMAS Methodology for Aeroacoustic Noise Source Definition," AIAA Paper 2005-2960, May 2005.

[23] Brooks, T. F. and Humphreys, W. M., "Extension of DAMAS Phased Array Processing for Spatial Coherence Determination (DAMAS-C)," AIAA Paper 2006-2654, May 2006.

[24] Dougherty, R. P., "Extensions of DAMAS and Benefits and Limitations of Deconvolution in Beamforming," AIAA Paper 2005-2961, May 2005.

[25] Huang, X., Bai, L., Vinogradov, I. and Peers, E., "Adaptive beamforming for array signal processing in aeroacoustic measurements," Journal of the Acoustical Society of America, No. 131, pp 2152-2161. March 2012.

[26] Cox, H., Zeskind, R. M. and Owen, M. M., "Robust adaptive beamforming," Institute of Electrical and Electronics Engineers (IEEE) Transactions on Acoustics, Speech, and Signal Processing, Vol. ASSP-35 No. 10, pp 1365-1367. October 1987.

[27] Li, J., Stoica, P. and Wang, W., "On Robust Capon Beamforming and Diagonal Loading," Institute of Electrical and Electronics Engineers (IEEE) Transactions on Signal Processing, Vol. 51, No. 7, pp 1702-1715. July 2003.

[28] Lord Rayleigh, F. R. S., "XXXI. Investigations in Optics, with special reference to the Spectroscope," The London, Edinburgh and Dublin Philosophical Magazine and Journal of Science. Fifth Series, Volume 8, No. 49, pp 261-274. October 1879.

[29] The Fokker Aircraft Page, URL: http://www.fokker-aircraft.info/f70general.htm [cited 16 April 2015]

[30] van der Goot, R., Hendriks, J., Scheper, K., Hermans, G., van der Wal, W. and Simons D. G., "A low cost, high resolution acoustic camera with a flexible microphone configuration,"Berlin Beamforming Conference, BeBeC 2012-08, 2012.